

Magnesium Cobaltate Nanowires@manganese Dioxide Nanoflakes Core-Shell Arrays on Graphene-Decorated Nickel Foam for High-Performance Supercapacitors

Xiangfeng Guan¹, Peihui Luo², Xiaoyan Li¹, Yunlong Yu¹, Yongjing Wang^{2,*}, Lin Zhuo¹, Dagui Chen^{1,*}

¹ College of Electronics and Information Science & Organic Optoelectronics Engineering Research Center of Fujian's Universities, Fujian Jiangxia University, Fuzhou, Fujian 350108, P.R. China

² College of Environment and Resources, Fuzhou University, Fuzhou 350108, P.R. China

*E-mail: yjwang03@fzu.edu.cn, dgchen@fjxu.edu.cn

Received: 1 January 2018 / Accepted: 17 February 2018 / Published: 10 April 2018

In this work, MgCo₂O₄ nanowires@manganese Dioxide nanoflakes core-shell arrays structure on graphene-decorated nickel foam were successfully prepared, which were featured by porous MnO₂ nanoflakes shell and one-dimensional MgCo₂O₄ nanowires core directly grown on the graphene. The morphologies of MgCo₂O₄ nanowires@manganese Dioxide nanoflakes core-shell arrays can be tuned by changing the hydrothermal reaction times. Due to the synergistic effect of graphene, MgCo₂O₄ nanowires, and MnO₂ nanoflakes, the optimized MgCo₂O₄ nanowires@manganese Dioxide nanoflakes core-shell arrays electrode materials exhibited excellent electrochemical performance such as high specific capacitances of 887.3 F g⁻¹ at a current density of 1 A g⁻¹ and good long-term cycling stability over 3000 cycles at a high current density of 10 A g⁻¹. The findings reported here clearly demonstrated that the core-shell arrays structure may be a promising candidate of high-performance electrode materials for supercapacitor.

Keywords: MgCo₂O₄; MnO₂; Core-shell arrays; Graphene; Supercapacitors

1. INTRODUCTION

In order to solve the worldwide energy shortage and environmental pollution problems caused by the increasing energy consumption, the development of green energy and energy storage devices has been widely concerned [1]. Supercapacitors are one of the most popular electrochemical devices for energy storage. It has good fast charge-discharge capability, stable cycle life, and good safety [2-4]. In spite of these advantages, the energy density of supercapacitors still needs to be further improved for wider range of applications. The key to solve the problem of low energy density of supercapacitors is to develop high-capacity active electrode materials, while maintaining good rate performance and

cycle stability [5]. A large number of studies have shown that the most effective strategy to improve electrode performance is to construct various kinds of active core-shell structure materials on the conductive substrate [6-10]. The multi-component core-shell structure can provide more electrochemical activity by improving the transmission path of electrons and ions, and can make full use of the synergy between different components, greatly improving the electrochemical performance of electrode materials [11].

In a variety of supercapacitor electrode materials, cobalt based materials have been widely studied because of their high electrochemical capacitance [12-14]. Magnesium cobaltate (MgCo_2O_4) is an important ternary oxide material, which has high theoretical capacitance (about 3122 F g^{-1}) [15]. Due to the limitation of low electric conductivity, MgCo_2O_4 with simple component structure shows relatively low specific capacitance at high current densities [16, 17]. Recently, much effort on the construction of multi-component structure for novel electrode materials has been devoted, which effectively improved the electric conductivity of electrode materials and thus promote the electrochemical performance. For example, $\text{MgCo}_2\text{O}_4/\text{rGO}$ composites have been prepared by a hydrothermal approach, which could deliver the specific capacitance of 570 F g^{-1} at 1 A g^{-1} with good capacitance retention after 5000 cycles [18]. MgCo_2O_4 nanocones have been grown on nickel foam by a hydrothermal synthesis route, which delivered the specific capacitance of 445.7 F g^{-1} at a high current density of 20 A g^{-1} [19]. These progresses made it clear that the electrochemical performance of MgCo_2O_4 electrode materials could be further improved by constructing complicate multi-components structure. Despite these great progresses, the electrochemical performances of MgCo_2O_4 -based electrode materials are still not satisfactory, especially its capacitance performance at high current densities need to be further improved.

In this work, we successfully synthesized MgCo_2O_4 nanowires@ MnO_2 nanoflakes core-shell arrays structure on graphene-decorated nickel foam by via chemical vapor deposition, hydrothermal, and heat-treatment methods. Due to the synergistic effect of graphene, MgCo_2O_4 nanowires, and MnO_2 nanoflakes, the optimized MgCo_2O_4 nanowires@ MnO_2 nanoflakes core-shell arrays electrode materials exhibited high specific capacitances, excellent rate capability, and good long-term cycling stability. To best of our knowledge, there have been no reports about MgCo_2O_4 @ MnO_2 core-shell nanostructure on graphene-decorated nickel foam for high-performance supercapacitor electrode materials. .

2. EXPERIMENTAL

2.1 Materials

Analytical grade chemicals of magnesium nitrate ($\text{Mg}(\text{NO}_3)_2 \cdot 6\text{H}_2\text{O}$), urea ($\text{CO}(\text{NH}_2)_2$), cobaltous nitrate ($\text{Co}(\text{NO}_3)_2 \cdot 6\text{H}_2\text{O}$), ammonium fluoride (NH_4F), and potassium permanganate (KMnO_4) were used as the starting materials without further purification.

2.2 Synthesis of graphene decorated nickel foam (G-NF)

G-NF was prepared by the chemical vapor deposition (CVD) method according to the previous report with slight modification [20]. Firstly, one piece of cleaned nickel foam (NF) was heated at 1000 °C for 60 min (heating rate of 30 °C/ min) in a quartz tube, with the flowing mixed gas of H₂ (10 sccm) and Ar (300 sccm). Secondly, CH₄ (60sccm) was loaded for another 15 min. Finally, the furnace was fast cooled down under a H₂/Ar flow and then G-NF was obtained.

2.3 Synthesis of MgCo₂O₄ nanowires@MnO₂ nanoflakes core-shell arrays on G-NF (MMO/G-NF)

In a typical synthesis procedure, about 0.3461 g Mg(NO₃)₂•6H₂O, 0.7858 g Co(NO₃)₂•6H₂O, 0.0666 g NH₄F, and 0.3243 g CO(NH₂)₂ were completely dissolved in 37 mL deionized water to form mixed solution. Then a piece of as-prepared G-NF (1 × 4 × 0.1 cm) was totally immersed into the mixed solution and placed into a 50 mL hydrothermal bomb to react at 130 °C for 5 h. The hydrothermally treated G-NF was cleaned, dried, and annealed in Ar flow at 400 °C for 2h to obtain MgCo₂O₄ nanowires arrays on G-NF (MgCo₂O₄/G-NF). Finally, the obtained MgCo₂O₄/G-NF was immersed into 37 mL KMnO₄ aqueous solution (0.03 M) and then placed into a 50 mL hydrothermal bomb to react at 160 °C for 3, 6, and 12 h to obtain different MMO/G-NF samples. According to the reaction times, the samples were named as MMO/G-NF-3h, MMO/G-NF-6h, and MMO/G-NF-12h. The typical synthesis process of MMO/G-NF is shown in Figure 1.

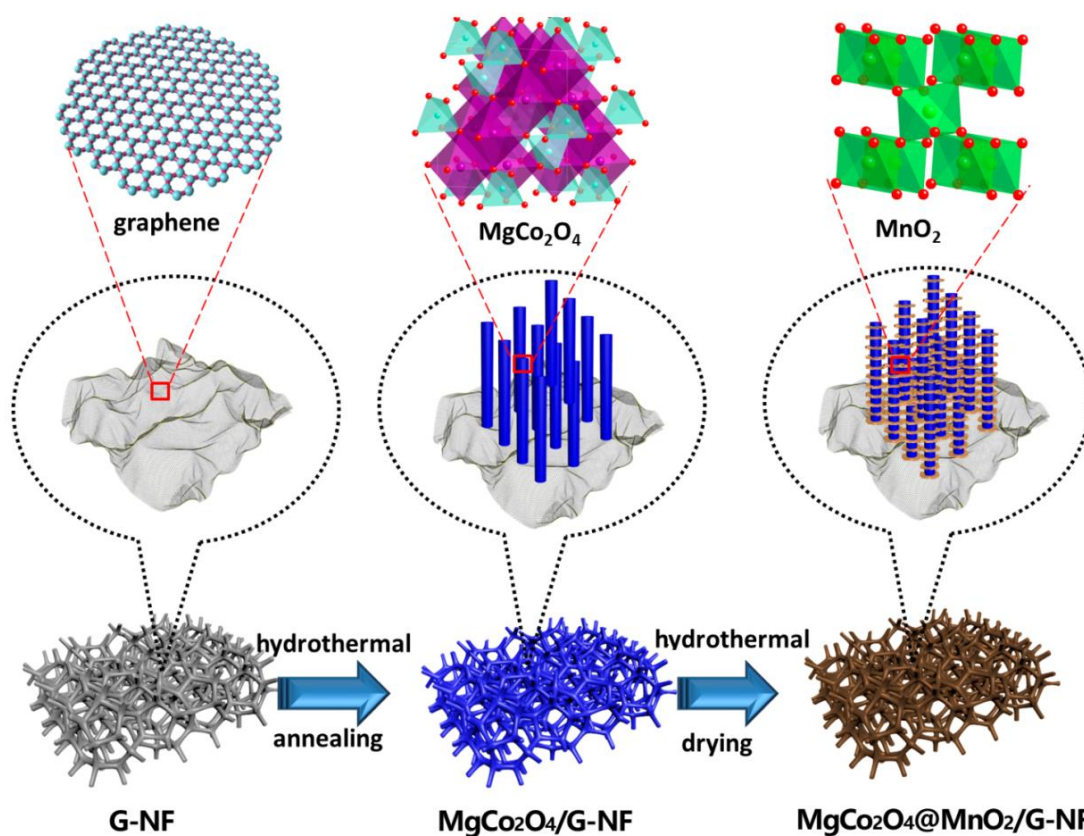


Figure 1. Synthetic schematic diagram for MgCo₂O₄ nanowires@MnO₂ nanoflakes core-shell arrays on graphene decorated nickel foam.

2.4 Materials characterization

The phase compositions were analyzed via x-ray diffraction (XRD). The morphologies and microstructures were determined using field emission scanning electron microscopy (FESEM) and transmission electron microscopy (TEM). Chemical compositions and valence states were determined by X-ray photoelectron spectroscopy (XPS).

2.5 Electrochemical characterization

The electrochemical performances of a three-electrode system were measured in 6.0 M KOH aqueous solution with an electrochemical workstation (CHI 660E). Pt and Ag-AgCl electrode were used as the counter and reference electrode, respectively. The as-prepared MM/G-NF samples were used as the working electrodes. Cyclic voltammetry (CV) was conducted at scan rates of 5, 10, 20, 50, and 100 mV s⁻¹. The galvanostatic charge-discharge (GCD) was measured at current densities of 1, 2, 5, 10, and 20 A g⁻¹. Electrochemical impedance spectroscopy (EIS) was conducted in the frequency range of 0.01-100 kHz with a potential amplitude of 5 mV.

3. RESULTS AND DISCUSSION

3.1 Structural and morphology analysis

The structural information of samples G-NF, MgCo₂O₄/G-NF, MMO/G-NF-6h was obtained by XRD, as shown in Figure 2a. For sample G-NF, two strong diffraction peaks between 40 and 55° (marked as #) and a weak diffraction peak around 26° (marked as ∇) were observed. The former two peaks are attributed to the planes of (111) and (200) of the metal nickel (No. 87-0712, JCPDS card). The latter weak peak can be indexed to the (002) plane of graphene [21]. For sample MgCo₂O₄/G-NF, the diffraction peaks (marked as ◆) indexed to (311) and (400) planes of MgCo₂O₄ phase (No. 81-0667, JCPDS card) can be seen, as well as the diffraction peaks attributed to metal nickel and graphene. Comparatively, for sample MMO/G-NF-6h, except for the diffraction peaks of metal nickel, graphene, and MgCo₂O₄ phase, the diffraction peaks (marked as ♣) attributed to the birnessite-type MnO₂ (No. 86-0666, JCPDS card) were observed. Figure 2b to 2d show the SEM images of samples NF, G-NF, and MgCo₂O₄/G-NF. For sample NF, the surface of nickel foam skeleton was smooth and 5-10 μm crystalline grains can be clearly seen (Figure 2b). Comparatively, for sample G-NF, a continuous graphene thin film homogeneously coated on the surface of nickel foam skeleton can be observed. The graphene film was so thin that the crystalline grains of metal nickel still can be seen (Figure 2c). For sample MgCo₂O₄/G-NF, the MgCo₂O₄ nanowires about 80 nm in width and 1 μm in length are found to homogeneously grow on the surface of G-NF. The MgCo₂O₄ nanowires were very dense, which makes graphene and crystalline grains of metal nickel hardly be observed.

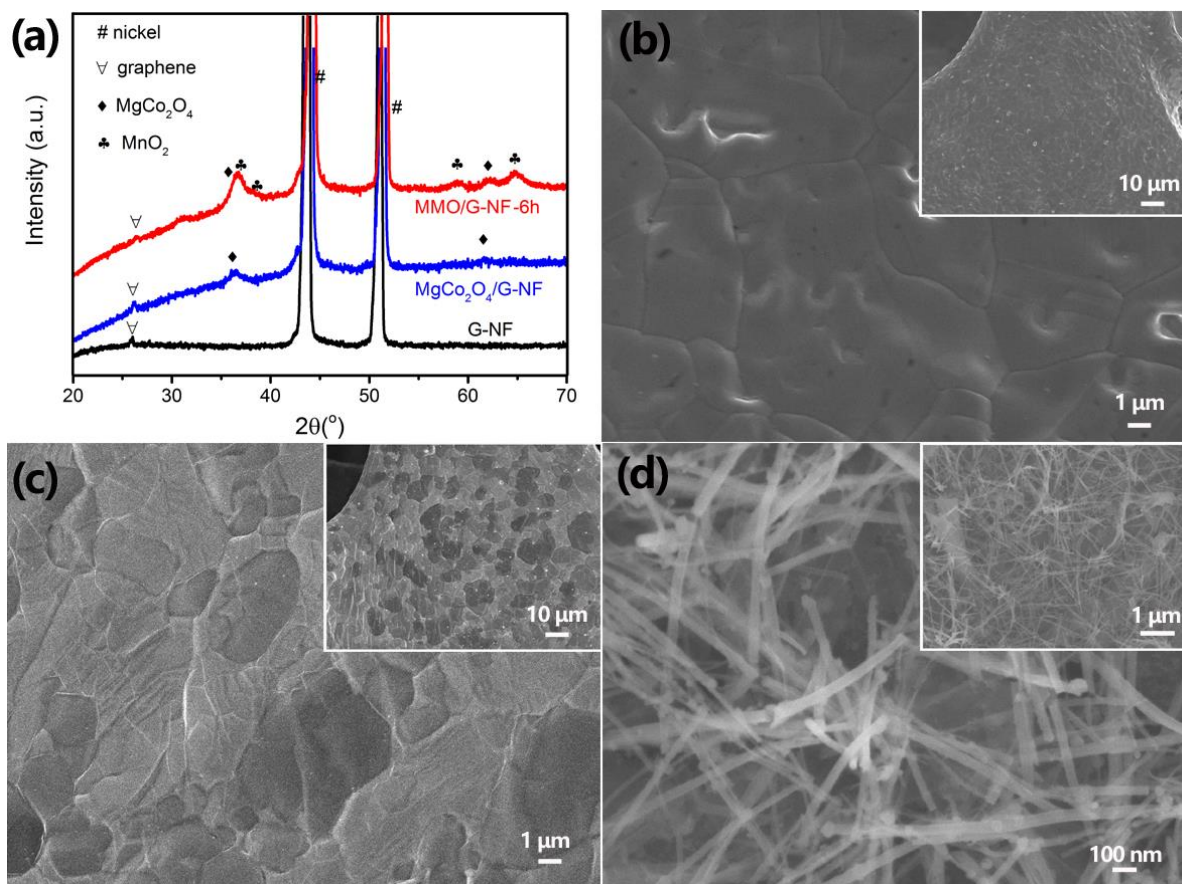


Figure 2. (a) XRD patterns of samples G-NF, $\text{MgCo}_2\text{O}_4/\text{G-NF}$, and $\text{MMO}/\text{G-NF-6h}$; SEM images of (b) nickel foam (NF); (c) graphene decorated nickel foam (G-NF); (d) MgCo_2O_4 nanowires arrays on G-NF ($\text{MgCo}_2\text{O}_4/\text{G-NF}$). The insets show low-magnification image.

Figure 3 shows the SEM and TEM images of MgCo_2O_4 nanowires@ MnO_2 nanoflakes core-shell arrays on G-NF ($\text{MMO}/\text{G-NF-6h}$). From the low-magnification SEM images in Figure 3a, it can be seen that the G-NF substrate was densely coated with nanowires arrays. With the side observation in Figure 3b, the thickness of the nanowire arrays are found to be about $2.5 \mu\text{m}$. From the closer observation in Figure 3c, it can be seen that the nanowires were interwoven to form porous net-like structure. High-magnification SEM image corresponding to marked area in Figure 3d clearly showed that the surface of nanowires are coated with nanoflakes. In comparison with the morphology of sample $\text{MgCo}_2\text{O}_4/\text{G-NF}$ in Figure 2d, one can easily deduced that the nanowires are MgCo_2O_4 phase and the nanoflakes are MnO_2 phase. Figure 3e shows the TEM image of a piece of nanoflakes, it can be seen that the nanoflakes are very thin and highly porous. The selected-area electron diffraction (SEAD) (the inset of Figure 3e) demonstrated the existence of diffuse diffraction rings, indicating highly polycrystalline nature of MnO_2 nanoflakes. The high-resolution TEM (HRTEM) showed the distinct interlayer spacings of 0.19 nm , which corresponds to the (-111) plane of the birnessite-type MnO_2 [22]. Moreover, pores with $5\text{-}10 \text{ nm}$ in diameters can be clearly seen.

To obtain detailed information on the surface composition and redox states of sample $\text{MMO}/\text{G-NF-6h}$, XPS measurements were carried out and the results are shown in Figure 4. The general survey

scan of the entire spectrum was calibrated with a C 1s standard (284.8 eV) before analysis. Figure 4a shows the survey spectrum of sample MMO/G-NF-6h, which mainly contain five core-levels peaks of Mg 1s, O 1s, C 1s, Co 2p, and Mn 2p. The Mg 1s peak (Figure 4b) is about 1303.1 eV, which agrees with the previous literature reports [23, 24]. The Co 2p spectrum (Figure 4c) shows the standard Co 2p_{3/2} and Co 2p_{1/2} peaks of MgCo₂O₄ at around 796 and 781 eV, respectively, thus implying that Co exists in both Co²⁺ and Co³⁺ state [25]. The associated satellite peaks are also observed, which agrees with previous reports [26]. Figure 4d shows the Mn 2p spectrum of the sample. It can be found that there are two intense peaks around 653.6 and 642.2 eV, which indicates the existence of Mn²⁺. In the O 1s spectrum (Figure 4e), the asymmetric O 1s peaks could be decomposed into three contributions of 529.8, 531.6, and 533.9 eV, which can be attributed to the metal-oxygen bond, oxygen in OH⁻ groups, and mixed composition containing Co²⁺, Co³⁺, and Mn²⁺ ions [21]. As shown in Figure 4f, the C 1s peak can be divided into three curves in the range of 283-290 eV [27].

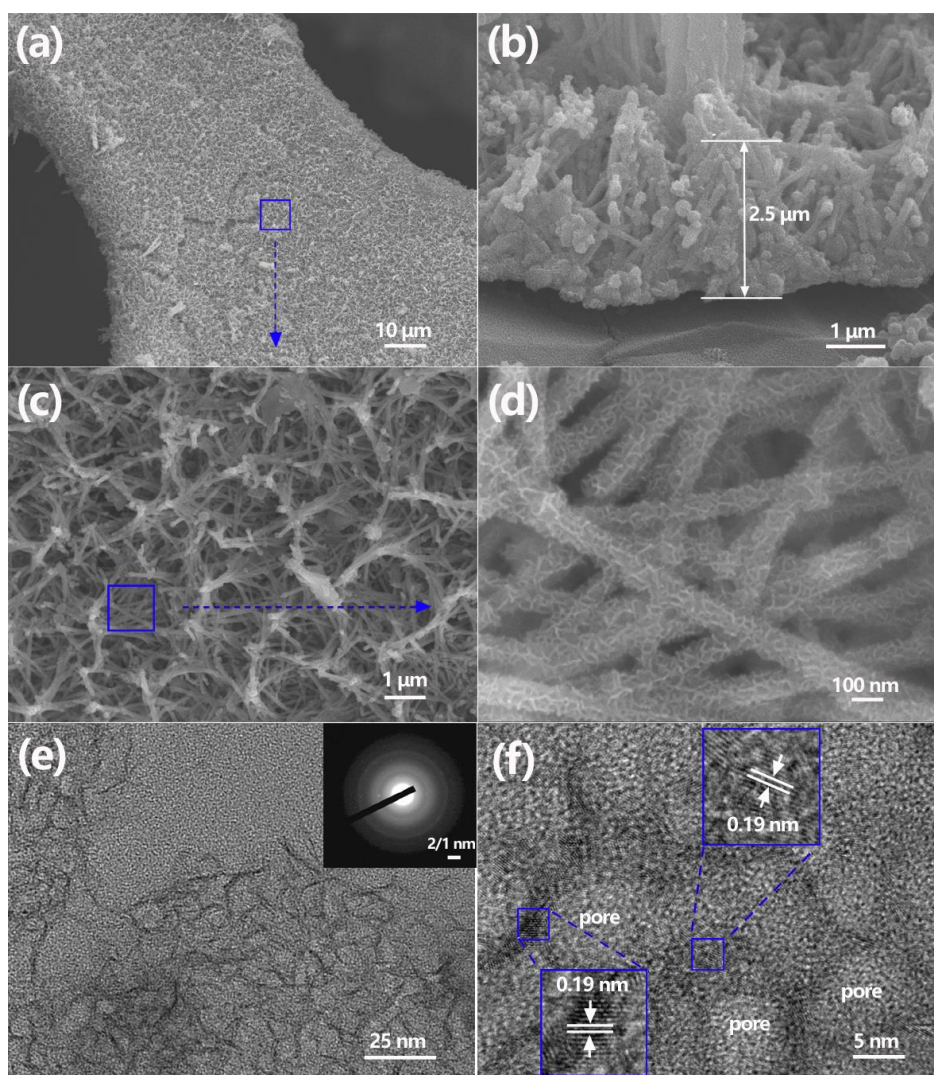


Figure 3. (a) Low-magnification SEM image of sample MMO/G-NF-6h; (b) the side view of MgCo₂O₄ @MnO₂ core-shell arrays; (c) Enlarged SEM image of the marked area in (a); (d) high-magnification SEM image of the marked area in (c); (e) TEM image of MnO₂ nanoflakes and the inset shows the SEAD pattern; (f) HRTEM images of MnO₂ nanoflakes.

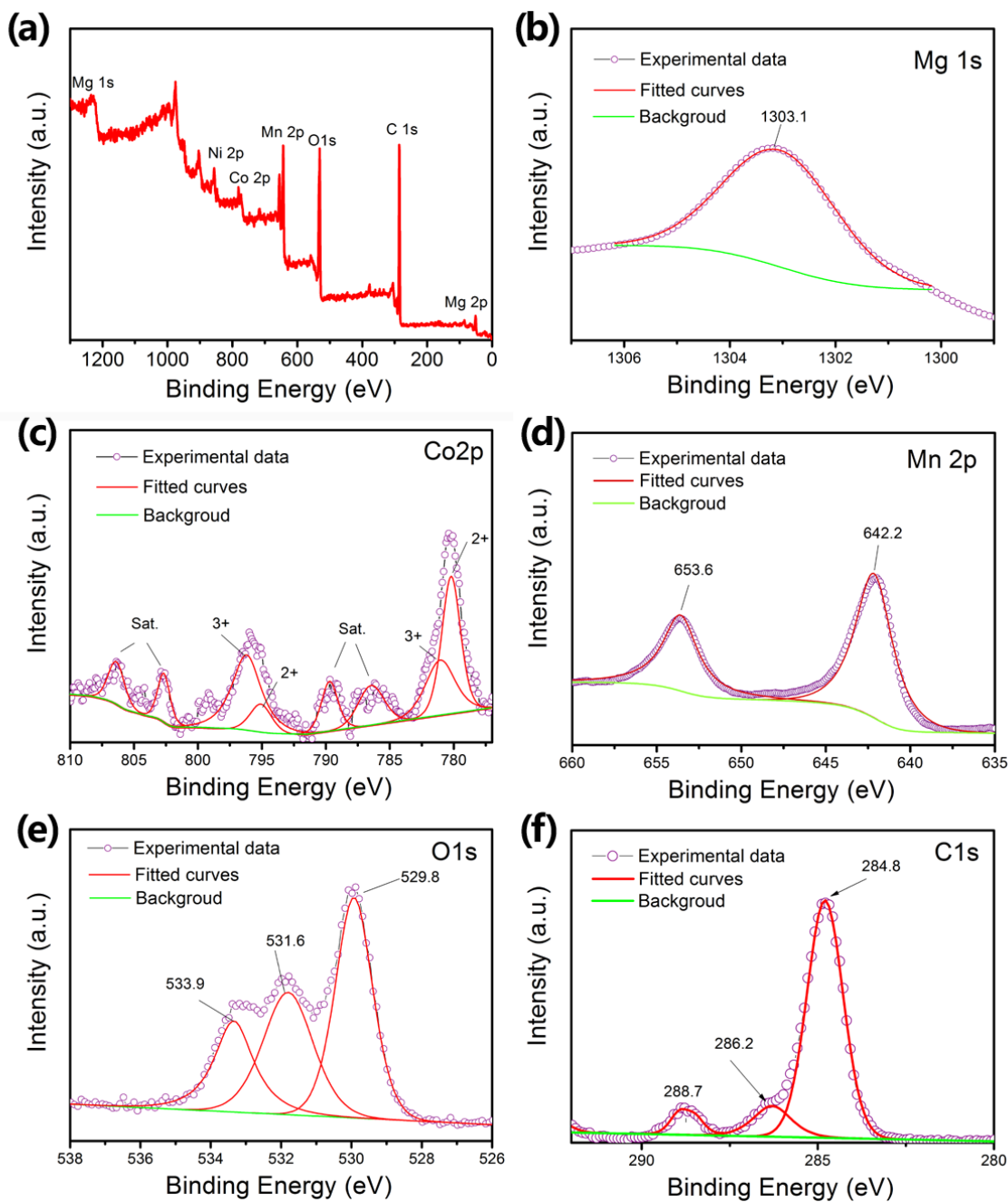


Figure 4. (a) Survey scan, (b) Mg 1s, (c) Co 2p, (d) Mn 2p, (e) O 1s, (f) C 1s binding energy spectra of sample MMO/G-NF-6h.

To investigate the effect of hydrothermal reaction times on the morphology of $\text{MgCo}_2\text{O}_4@ \text{MnO}_2$ core-shell arrays, several parallel experiments are performed. By changing the hydrothermal reaction times, different morphologies of $\text{MgCo}_2\text{O}_4@ \text{MnO}_2$ core-shell arrays can be obtained (Figure 5). When the hydrothermal reaction time is 3 h (sample MMO/G-NF-3h), the MnO_2 nanoflakes are homogeneously distributed on the surface of MgCo_2O_4 nanowires, indicating the formation of MgCo_2O_4 nanowires@ MnO_2 nanoflakes core-shell structure (Figure 5a and 5d). The diameters of core-shell nanowires are about 100 nm, which is larger than those of MgCo_2O_4 nanowires

(Figure 2d). When the hydrothermal reaction times increased to 6 h (sample MMO/G-NF-6h), the morphology of MgCo_2O_4 nanowires@ MnO_2 nanoflakes core-shell structure are also clearly observed, except that the diameters of core-shell nanowires increased to about 120 nm (Figure 5b and 5e). Apparently, the increased in diameters is ascribed to the growth of MnO_2 nanoflakes. When the hydrothermal reaction times prolonged to 12 h (sample MMO/G-NF-12h), the MgCo_2O_4 nanowires@ MnO_2 nanoflakes core-shell structure was hardly observed because of the coverage by overgrown MnO_2 nanoflakes.

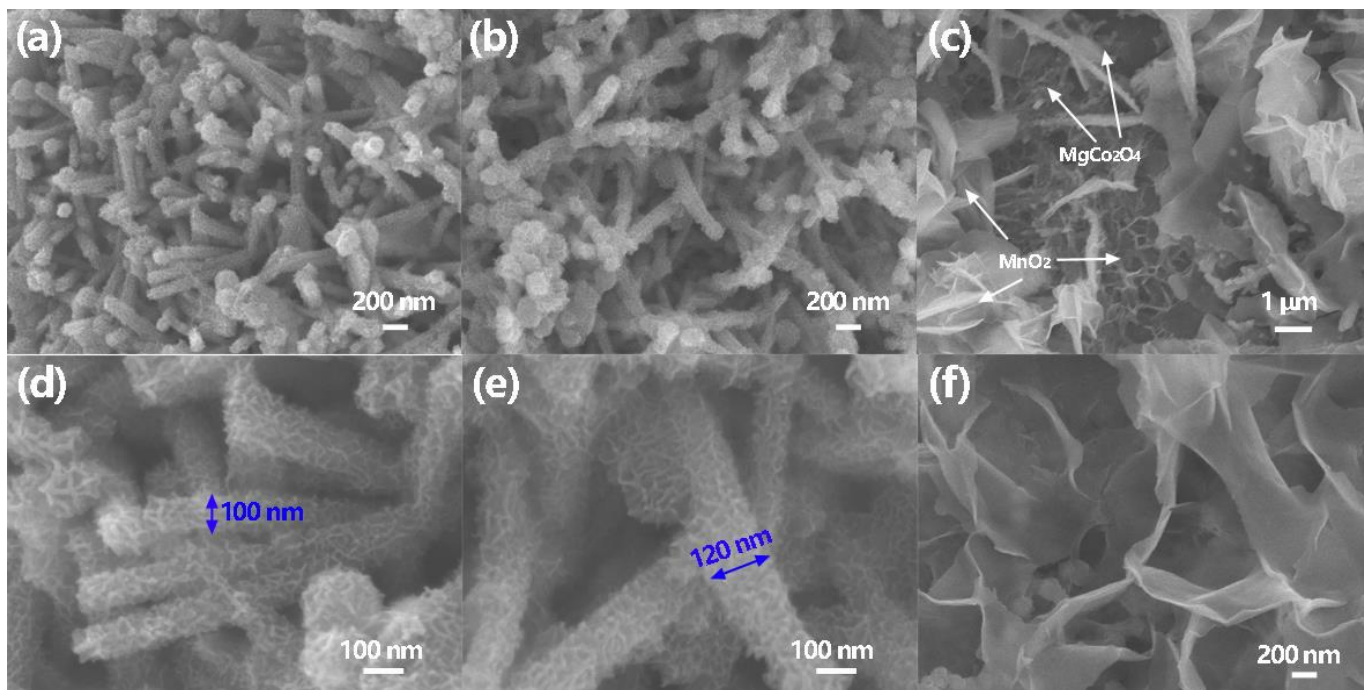


Figure 5. Low-magnification SEM images of the samples: (a) MMO/G-NF-3h; (b) MMO/G-NF-6h; (c) MMO/G-NF-12h and high-magnification SEM images of the samples: (d) MMO/G-NF-3h; (e) MMO/G-NF-6h; (f) MMO/G-NF-12h.

The as-prepared MgCo_2O_4 @ MnO_2 core-shell arrays/G-NF samples were evaluated as supercapacitor electrodes. Figure 6a shows the CV curves measured at a scan rate of 5 mV s^{-1} with the voltage range of 0-0.5 V. The distinct redox peaks originated from the faradaic redox reactions can be observed for all three samples [28]. The areas of CV curves of sample MMO/G-NF-6h and MMO/G-NF-12h are comparable, which are larger than that of sample MMO/G-NF-3h, representing higher capacitance. Figure 6b to 6d shows the CV curves at different scanning rates for samples MMO/G-NF-3h, MMO/G-NF-6h, and MMO/G-NF-12h, respectively. When the scan rates increase from 5 to 100 mV s^{-1} , the CV curves for all samples exhibit enlarged areas as well as similar curve shape, which indicates fast redox reactions enabled by the unique MgCo_2O_4 nanowires@ MnO_2 nanoflakes core-shell structure on G-NF. It is noted that sample MMO/G-NF-6h shows the highest curve areas among three samples at relatively high scanning rates, such as 50 mV s^{-1} and 100 mV s^{-1} . Thus we anticipated that sample MMO/G-NF-6h could exhibit good high-rate electrochemical performance.

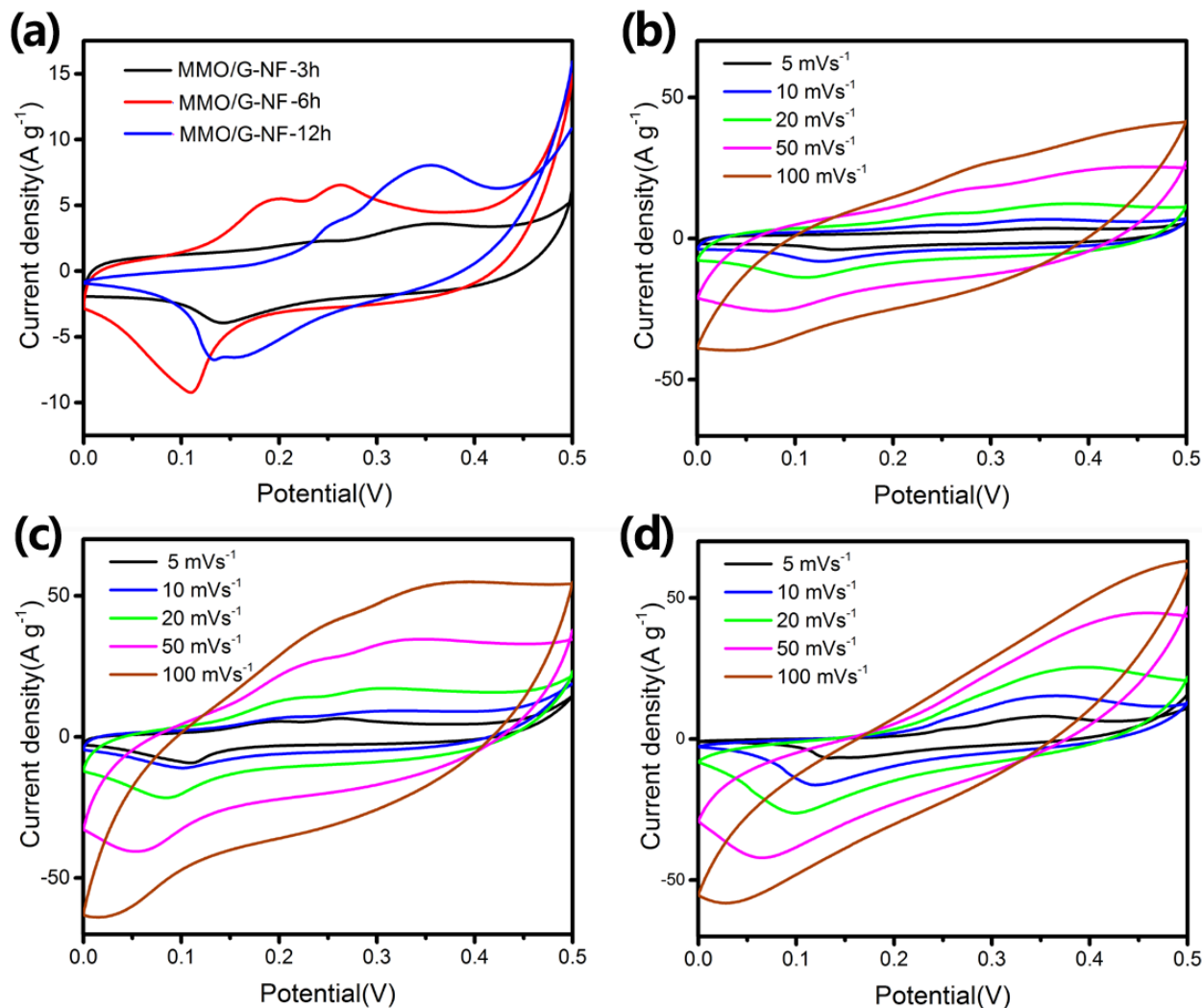


Figure 6. (a) CV curves of all samples at a scan rate of 5 mVs^{-1} ; and CV curves at varied scan rates of all samples: (b) MMO/G-NF-3h, (c) MMO/G-NF- 6h, (d) MMO/G-NF-12h.

Figure 7 shows the typical galvanostatic charge-discharge (GCD) curves of the three samples at current densities of 1, 5, 10, and 20 A g^{-1} . Among three samples, sample MMO/G-NF-3h shows the shortest charge-discharge times, which indicates that sample MMO/G-NF-3h possesses the lowest capacitance. It is interesting to see that sample MMO/G-NF-6h exhibited shorter charge-discharge times in comparison with sample MMO/G-NF-12h at the relatively low current densities of 1 and 5 A g^{-1} ; while possessed longer charge-discharge times at the relatively high current densities of 10 A g^{-1} and 20 A g^{-1} . The specific capacitance (C_s) can be calculated with the equation $C_s = I\Delta t / (m\Delta V)$ [29], where I , Δt , m , ΔV represents the discharge current, time, the mass of active materials, and the potential drop, respectively. The calculated specific capacitances of three samples are listed in Table 1.

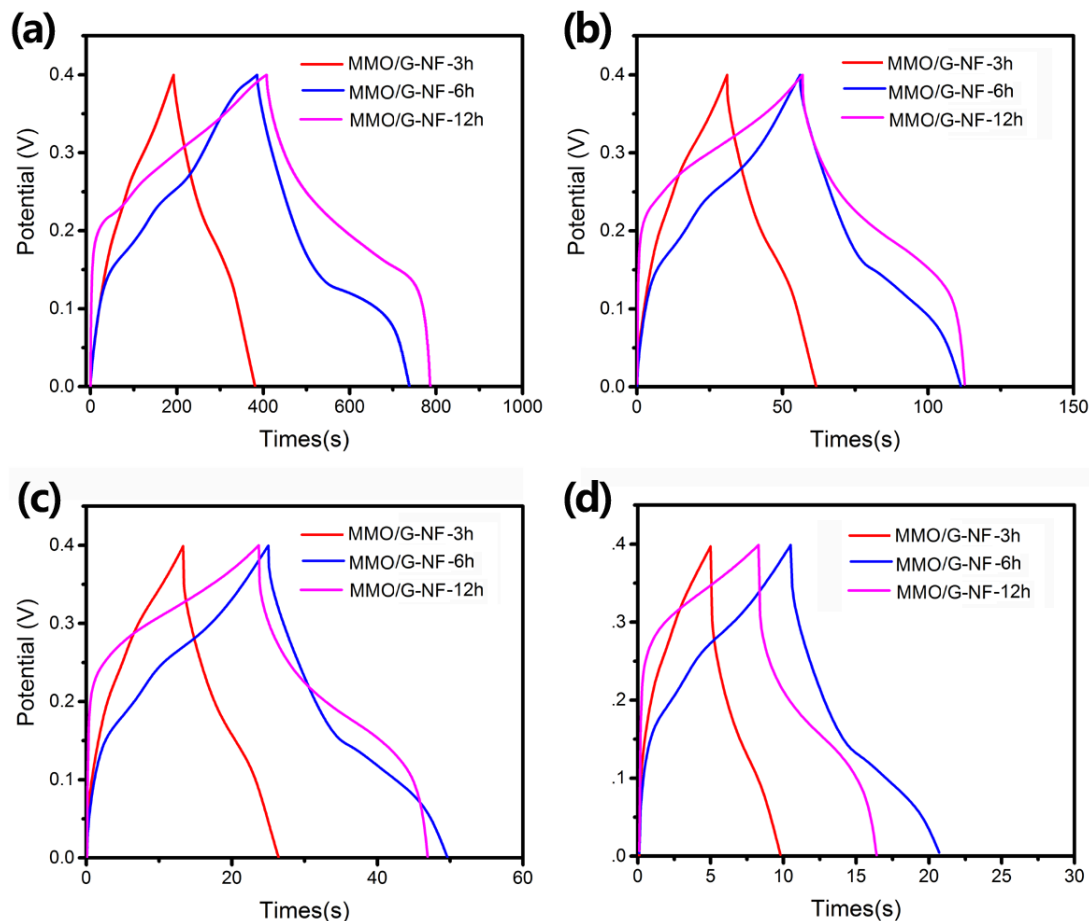


Figure 7. Galvanostatic charge–discharge (GCD) curves of all electrodes at different current density: (a) 1 A g⁻¹, (b) 5 A g⁻¹, (c) 10 A g⁻¹, (d) 20A g⁻¹.

It is seen that sample MMO/G-NF-6h delivered the specific capacitances of 887.3, 784.5, 690.0, 615.1, and 510.4 F g⁻¹ at the current densities of 1, 2, 5, 10, and 20 A g⁻¹, respectively. Comparatively, sample MMO/G-NF-12h exhibited the specific capacitances of 953.8, 848.1, 696.3, 580.1, and 405.2 F g⁻¹ at the current densities of 1, 2, 5, 10, and 20 A g⁻¹, respectively. Apparently, sample MMO/G-NF-6h displayed the better electrochemical performance at high current densities than sample MMO/G-NF-12h, which is in accordance with the CV results shown in Figure 6.

Table 1. Electrochemical performance of as-prepared MgCo₂O₄@MnO₂ arrays/G-NF samples

Electrode	Specific capacity (F g ⁻¹)				
	1 A g ⁻¹	2 A g ⁻¹	5 A g ⁻¹	10 A g ⁻¹	20 A g ⁻¹
MMO/G-NF-3h	472.5	437.5	382.5	327.5	240
MMO/G-NF-6h	887.3	784.5	690.0	615.1	510.4
MMO/G-NF-12h	953.8	848.1	696.3	580.1	405.2

Figure 8 shows the comparison of the electrochemical performance (specific capacitance versus specific current) of as-prepared $\text{MgCo}_2\text{O}_4@\text{MnO}_2$ core-shell arrays/G-NF samples with other MgCo_2O_4 -based supercapacitor electrode materials. It can be seen that our $\text{MgCo}_2\text{O}_4@\text{MnO}_2$ core-shell arrays/G-NF samples exhibited high specific capacitance and good high-rate performance. In particular, the sample MMO/G-NF-6h in this work exhibit outstanding high-rate electrochemical performance with the highest specific capacitance of 510.4 F g^{-1} at a large current density of 20 Ag^{-1} , demonstrating superiority than other MgCo_2O_4 -based supercapacitor electrode materials reported in literatures, including MgCo_2O_4 hierarchical architectures[15], MgCo_2O_4 nanoparticles [16], MgCo_2O_4 nanorods [17], $\text{MgCo}_2\text{O}_4/\text{rGO}$ [18], and MgCo_2O_4 nanocone/nickel foams[19], MgCo_2O_4 cuboidal microcrystals [30].

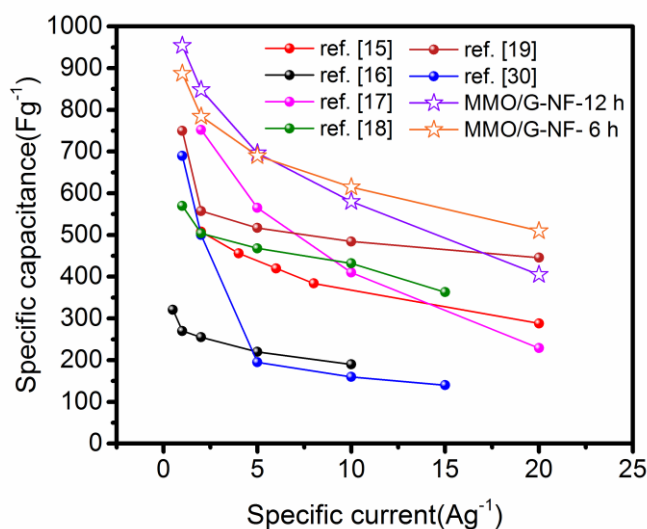


Figure 8. Comparison of the electrochemical performance of as-prepared $\text{MgCo}_2\text{O}_4@\text{MnO}_2$ core-shell arrays/G-NF samples with other MgCo_2O_4 -based supercapacitor electrode materials (specific capacitance versus specific current)

Since the long-term cycling performance of supercapacitor electrode is an important index for the practical application, the as-prepared $\text{MgCo}_2\text{O}_4@\text{MnO}_2$ core-shell arrays/G-NF samples were cycled at a current density of 10 A g^{-1} for 3000 times, as shown in Figure 9a. Among three samples, sample MMO/G-NF-6h exhibited robust specific capacitance and excellent cycling stability, which delivered the highest specific capacitance of 529.1 F g^{-1} and the highest capacitance retention ratio of 86.0 % after being cycled 3000 times. As can be seen in Table 2, the specific capacitance of sample MMO/G-NF-6h after being cycled 3000 times at the current density of 10 A g^{-1} is superior to that of MgCo_2O_4 hierarchical architectures cycled at the same current density, and even better than those of MgCo_2O_4 based materials cycled at smaller current densities that are more beneficial to obtain large capacity. Figure 9b to 9d shows the SEM images of sample MMO/G-NF-6h after being cycled for 3000 times. It is seen that $\text{MgCo}_2\text{O}_4@\text{MnO}_2$ core-shell structure still remained homogeneously distributed on nickel foam skeleton (Figure 9b). The morphology of nanowires did not obviously change (Figure 9c) and the nanoflakes can be seen on the surface of nanowires (Figure 9d), indicating the structure stability of MgCo_2O_4 nanowires@ MnO_2 nanoflakes core-shell structure.

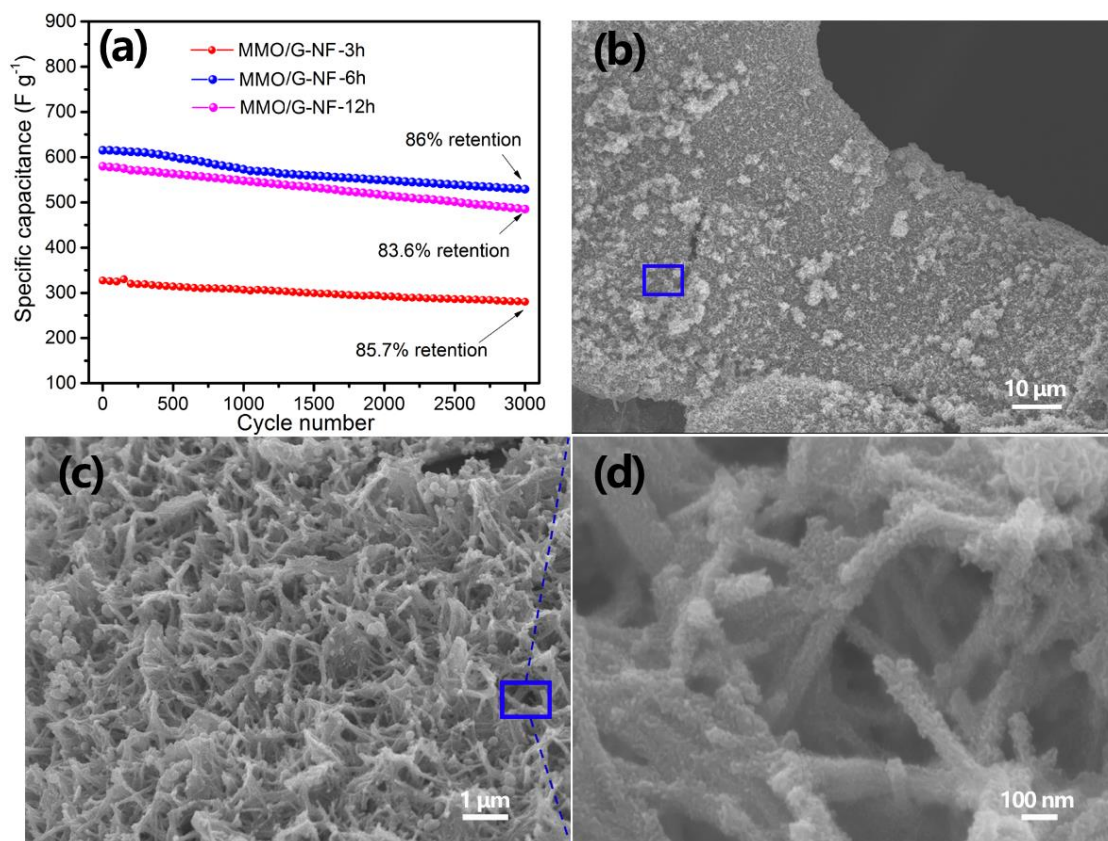


Figure 9. (a) cycling performance of as-prepared $\text{MgCo}_2\text{O}_4@\text{MnO}_2$ core-shell arrays/G-NF samples and SEM images of the sample MMO/G-NF-6h after being cycled for 3000 times: (b) low-magnification, (c) high-magnification, and (d) enlarged images of the marked area in (c).

Table 2. Cycling performance of sample MMO/G-NF-6h and previously reported MgCo_2O_4 based materials

Materials	Preparation method	Current density	First Capacitance	Cycle number	Remaining capacitance	References
MgCo_2O_4 hierarchical architectures	Hydrothermal-heat treatment	10 A g^{-1}	$\sim 450 \text{ F g}^{-1}$	2000	$\sim 431 \text{ F g}^{-1}$	[15]
MgCo_2O_4 nanoparticles	Molten salt	2 A g^{-1}	$\sim 220 \text{ F g}^{-1}$	2000	344 F g^{-1}	[16]
MgCo_2O_4 nanocone/nickel foams	Hydrothermal-heat treatment	1 A g^{-1}	750 F g^{-1}	1000	630 F g^{-1}	[19]
MgCo_2O_4 cuboidal microcrystals	Hydrothermal-heat treatment	5 A g^{-1}	380 F g^{-1}	3000	415 F g^{-1}	[30]
MMO/G-NF-6h	CVD-hydrothermal-heat treatment	10 A g^{-1}	615.1 F g^{-1}	3000	529.1 F g^{-1}	This work

Figure 10 shows EIS spectra of the $\text{MgCo}_2\text{O}_4@\text{MnO}_2$ core-shell arrays/G-NF samples. The EIS curves are composed of a semicircle and an oblique line. According to the equivalent circuit (inset in Figure 10), R_{ct} is the resistance of Faradic charge transfer; C_L is double layer capacitance; Z_w is the Warburg impedance, R_s is the internal resistance of the solution [31]. From the intersection value of the semicircle at real part Z' , the value of R_s can be obtained. It is apparent that sample MMO/G-NF-6h has the lowest value of R_s among three electrodes and more ideal slope of straight line, which indicates that sample MMO/G-NF-6h has fast migration of charge carriers. The superior electrochemical performance of sample MMO/G-NF-6h can be ascribed to the synergistic effect of different components including graphene, MgCo_2O_4 nanowires, and MnO_2 nanoflakes: (i) The graphene can improve the electron transportation of electrode materials, and also play as a buffer layer between MgCo_2O_4 nanowires@ MnO_2 nanoflakes core-shell structure and the nickel skeleton, which effectively strengthened the mechanical adhesion and improve the cycling stability [32]. (ii) The direct growth of the MgCo_2O_4 core nanowires on graphene could ensure every nanowire participates in the ultrafast electrochemical reaction at high current densities. (iii) The porous MnO_2 nanoflakes shell grown on the surface of structure MgCo_2O_4 nanowire can promote ions penetration and shorten transport path of electron and ion, which improve the capacitance of electrode materials. It seems that the thickness of MnO_2 shell is crucial for the electrochemical performance of the $\text{MgCo}_2\text{O}_4@\text{MnO}_2$ core-shell arrays/G-NF samples. For sample MMO/G-NF-3h, the MnO_2 shell was relatively thin that could not effectively form interconnected MnO_2 network, the transport path of electron and ion were not fully shortened. For sample MMO/G-NF-12h, the MnO_2 nanoflakes were overgrown on the MgCo_2O_4 nanowires, which made the structures unstable and lowered the high-rate electrochemical performance. Consequently, sample MMO/G-NF-6h has excellent high-rate electrochemical performance and good long-term cycling performance, which can be ascribed to the optimized $\text{MgCo}_2\text{O}_4@\text{MnO}_2$ core-shell arrays structure.

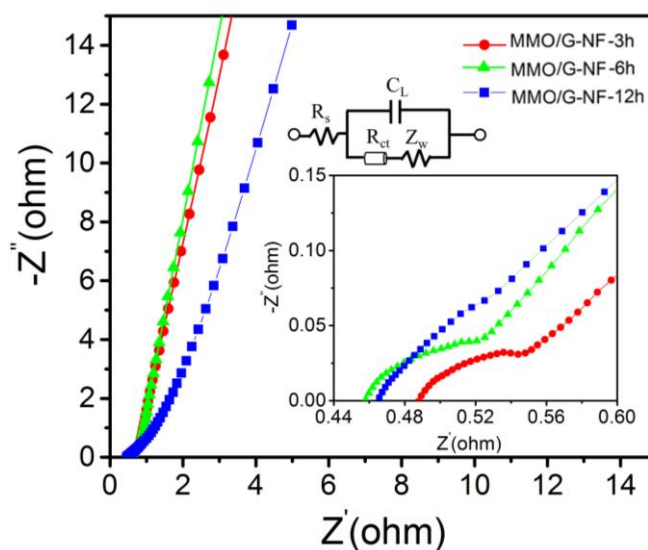


Figure 10. EIS of the MgCo_2O_4 nanowires@ MnO_2 nanoflakes arrays/G-NF electrodes

4. CONCLUSIONS

In summary, MgCo₂O₄ nanowires@MnO₂ nanoflakes core-shell arrays structure on graphene-decorated nickel foam were successfully prepared. The XRD, SEM, and TEM results indicated that the core components are MgCo₂O₄ nanowires which are about 80 nm in width and 1 μm in length and the shell components are porous MnO₂ nanoflakes. The XPS results confirmed the co-existence of Mg²⁺, Co²⁺, Co³⁺, and Mn²⁺ in the core-shell arrays. The electrochemical measurements showed that the optimized MgCo₂O₄ nanowires@MnO₂ nanoflakes core-shell arrays electrode materials delivered the specific capacitances of 887.3, 784.5, 690.0, 615.1, and 510.4 F g⁻¹ at the current densities of 1, 2, 5, 10, and 20 A g⁻¹, respectively. And the core-shell arrays electrode materials also exhibited excellent long-term cycling stability at a high current density of 10 A g⁻¹, which delivered the specific capacitance of 529.1 F g⁻¹ with the capacitance retention ratio of 86.0 % after being cycled 3000 times. These remarkable electrochemical performances indicated that the core-shell arrays electrode materials could be a promising candidate for high-performance supercapacitor.

ACKNOWLEDGEMENTS

The financial supports of the Natural Science Foundation of Fujian Province (2017J01676, 2017J01677, 2017J01733, 2015J01654, 2015J05091, 2015J01632), the National Natural Science Foundation of China (61376002, 51503036), the Key Research Foundation for Young Scholars of Fujian Education Department of China (JZ160484, JZ160486), and Fujian Education Department of China (JAT160558) are gratefully acknowledged.

References

1. X. Li, B. Q. Wei, *Nano Energy*, 2 (2013) 159.
2. B. Saravanakumar, S. P. Ramachandran, G. Ravi, V. Ganesh, R. K. Guduru, R. Yuvakkumar, *Mater. Res. Expre.*, 5 (2018) 015504.
3. Y. Yan, B. Li, W. Guo, H. Pang, H. G. Xue, *J. Power Sources*, 329 (2016) 148.
4. L. L. Liu, Z. Q. Niu, J. Chen, *Chem. Soc. Rev.*, 45 (2016) 4340.
5. M. F. Ei-Kady, Y. L. Shao, R. B. Kaner, *Nature Rev. Mater.*, 1 (2016) 16033.
6. L. X. Zhou, Y. He, C. P. Jia, V. Pavlinek, P. Saha, Q. L. Cheng, *Nanomater.*, 7 (2017) 273.
7. X. Bai, Q. Liu, J. Y. Liu, H. S. Zhang, Z. S. Li, X. Y. Jing, P. L. Liu, J. Wang, R. M. Li, *Chem. Eng. J.*, 315 (2017) 35.
8. V. H. Nguyen, C. Lamiel, J. J. Shim, *Mater. Lett.*, 170 (2016) 105.
9. J. S. Xu, Y. D. Sun, M. J. Lu, L. Wang, J. Zhang, J. H. Qian, E. J. Kim, *J. All. Comp.*, 717 (2017) 108.
10. Y. Y. Zhang, J. X. Wang, J. H. Ye, P. P. Wan, H. M. Wei, S. Q. Zhao, T. F. Li, S. Hussain, *Ceram. Inter.*, 42 (2016) 14976.
11. M. Kuang, X. Y. Liu, F. Dong, Y. X. Zhang, *J. Mater. Chem. A*, 3 (2015) 21528.
12. R. Samal, B. Dash, C. K. Sarangi, K. Sanjay, T. Subbaiah, G. Senanayake, M. Minakshi, *Nanomater.*, 7 (2017) 356.
13. X. F. Guan, Y. L. Yu, X. Y. Li, D. G. Chen, P. H. Luo, Y. Zhang, S. X. Guo, *Mater. Res. Expre.* 5 (2018) 015002.
14. Q. Yang, Z. Y. Lu, X. M. Sun, J. F. Liu, *Sci. Rep.*, 3 (2013) 3537.

15. J. S. Xu, L. Wang, J. Zhang, J. H. Qian, J. Liu, Z. Q. Zhang, H. D. Zhang, X. Y. Liu, *J. All. Comp.*, 688 (2016) 933.
16. S. G. Krishnan, M. V. Reddy, M. Harilal, B. J. Vidyadharan, I. I. Misnon, M. H. A. Rahim, J. Ismail, R. Jose, *Electrochimi. Acta*, 161 (2015) 312.
17. M. Silambarasan, P. S. Ramesh, D. Geetha, *J. Mater. Sci.: Mater. Electron.*, 28 (2017) 6880.
18. S. G. Krishnan, M. Harilal, A. Yar, B. L. Vijayan, J. O. Dennis, M. M. Yusoff, R. Jose, *Electrochimi. Acta*, 243 (2017) 119.
19. L. F. Cui, L. H. Huang, M. Ji, Y. G. Wang, H. C. Shi, Y. H. Zuo, S. F. Kang, *J. Power. Sources*, 333 (2016) 118.
20. Q. F. Wang, J. Xu, X. F. Wang, B. Liu, X. J. Hou, G. Yu, P. Wang, D. Chen, G. Z. Shen, *ChemElectroChem*, 1 (2014) 559.
21. H. Chen, C. K. Hsieh, Y. Yang, X. Y. Liu, C. H. Lin, C. H. Tsai, Z. Q. Wen, F. Dong, Y. X. Zhang, *ChemElectroChem.*, 4 (2017) 2414.
22. D. Ji, H. Zhou, J. Zhang, Y. Y. Dan, H. X. Yang, A. H. Yuan, *J. Mater. Chem. A*, 4 (2016) 8283.
23. F. Esaka, T. Nojima, H. Udono, M. Magara, H. Yamamoto, *Surf. Interface Anal.*, 48 (2016) 432.
24. J. Zhang, Y. H. Wang, J. S. Zheng, F. Huang, D. G. Chen, Y. Z. Lan, G. Q. Ren, Z. Lin, C. Wang, *J. Phys. Chem. B*, 111(2007) 1449.
25. P. Stelmachowski, G. Maniak, J. Kaczmarczyk, F. Zasada, W. Piskorz, A. Kotarba, Z. Sojka, *Appl. Catal. B: Environ.*, 146 (2014) 105.
26. Z. Y. Pu, H. Zhou, Y. F. Zheng, W. Z. Huang, X. N. Li, *Appl. Surf. Sci.*, 410 (2017) 14.
27. C. Zhang, X. P. Geng, S. L. Tang, M. S. Deng, Y. W. Du, *J. Mater. Chem. A*, 5 (2017) 5912.
28. M. Kim, J. Yoo, J. Kim, *J. All. Compd.*, 710 (2017) 528.
29. Y. H. Li, S. Chang, X. L. Liu, J. C. Huang, J. L. Yin, G. L. Wang, D. X. Cao, *Electrochimi. Acta*, 85 (2012) 393.
30. S. G. Krishnan, M. Harilal, I. I. Misnon, M. V. Reddy, S. Adams, R. Jose, *Ceram. Inter.*, 43 (2017) 12270.
31. L. Xu, Y. Zhao, J.B. Lian, Y. G. Xu, J. Bao, J. X. Qiu, L. Xu, H. Xu, M.Q. Hua, H. M. Li, *Energy*, 123 (2017) 296.
32. C. F. Zhang, J. S. Yu, *Chem. Eur. J.*, 22 (2016) 4422.

© 2018 The Authors. Published by ESG (www.electrochemsci.org). This article is an open access article distributed under the terms and conditions of the Creative Commons Attribution license (<http://creativecommons.org/licenses/by/4.0/>).